

1 Energetic Electron Precipitation from the Radiation Belts: Geomagnetic and Solar  
2 Wind Proxies for Precipitation Flux Magnitudes

3 Malcolm Crack<sup>1</sup>, Craig J. Rodger<sup>1</sup>, Mark A. Clilverd<sup>2</sup>, Aaron T. Hendry<sup>1,2</sup>, and Jean-Andre  
4 Sauvaud<sup>3</sup>

5 <sup>1</sup>Physics Department, University of Otago, Dunedin, New Zealand.

6 <sup>2</sup>British Antarctic Survey (UKRI-NERC), Cambridge, United Kingdom.

7 <sup>3</sup>Institut de Recherche en Astrophysique et Planétologie (IRAP), Toulouse, France.

8

9 Corresponding author: Mark Clilverd ([macl@bas.ac.uk](mailto:macl@bas.ac.uk))

10 **Key Points:**

- 11
- 12 • The suitability of geomagnetic and solar wind indices for use as proxies for energetic  
electron precipitation flux variations are examined
  - 13 • For medium energy electron precipitation (i.e., >100 keV), the best proxies were found to  
14 be either the Ap or Dst geomagnetic indices
  - 15 • For relativistic energy electron precipitation (i.e., >700 keV), the best proxies were  
16 identified as the Kp or AE geomagnetic indices
- 17

18

**19 Abstract**

20 Previously the geomagnetic Ap index has been used as a proxy to produce empirical energetic  
21 electron precipitation (EEP) forcing representations suitable for incorporation into coupled-  
22 climate model runs. The long-running Ap index has the advantage that it allows descriptions of  
23 EEP to be made for periods outside the current satellite era, but its suitability has not been  
24 checked against other reasonable proxies. In this study 3 different satellite electron precipitation  
25 datasets (DEMETER, POES, and SAMPEX) are used to examine the suitability of a variety of  
26 geomagnetic and solar wind proxies to represent EEP flux in different energy ranges. Analysis  
27 was undertaken using indices at their fundamental timescales (typically minutes or hours). For  
28 medium energy electron precipitation (i.e., >100 keV), the best proxy is found to be either Ap or  
29 Dst. For relativistic energy electron precipitation (i.e., >700 keV), the best proxy is Kp or AE,  
30 the latter suggesting a connection to substorm activity. The identification of the Ap index as one  
31 of the best proxies for medium energy EEP supports the approach taken by van de Kamp et al.  
32 (2016). An EEP forcing capability based on Ap was developed by those authors for inclusion as  
33 a solar forcing factor in the Coupled Model Intercomparison Project Phase 6 of the World  
34 Climate Research Programme.

**35 Plain Language Summary**

36 In order to determine the effect of energetic particle forcing on the Earth's atmosphere over  
37 decadal timespans it has been necessary to develop models of energetic electron precipitation  
38 (EEP) based on long time-series geomagnetic indices. This has been done using the geomagnetic  
39 index Ap which was recommended for use for EEP forcing in the Coupled Model  
40 Intercomparison Project Phase 6 of the World Climate Research Programme. However, in that  
41 process Ap was not selected as a proxy for EEP based on its merit, but rather for convenience.  
42 Here we use the EEP measurements from 3 different satellite datasets, 2 individual spacecraft  
43 and 1 constellation. We look over a range of particle detector configurations to test for the 'best'  
44 proxy; investigating both geomagnetic and solar wind parameters. In all we tested seven different  
45 indices to see how good they were as proxies for EEP and found that for medium energy  
46 electrons the best proxies were Ap, and Dst – both geomagnetic indices. For higher energies,  
47 relativistic electron precipitation is best proxied by Kp or AE. This should be considered if and  
48 when any solar forcing factors are expanded into these relativistic energies for EEP.

49

**50 1 Introduction**

51 Descriptions of solar forcing terms that are recommended for use in coupled-climate  
52 model runs have been summarised by Matthes et al. (2017). The forcing terms include solar  
53 irradiance, tropical ozone variations, and energetic particle precipitation. Particle precipitation is  
54 one of the routes by which the Sun can link to the climate system; energetic electrons and  
55 protons can change atmospheric chemistry through the production of reactive species in the  
56 upper atmosphere (Brasseur and Solomon, 2005). The Matthes et al. recommendations were  
57 published in order to facilitate the inclusion of solar forcing in the Coupled Model  
58 Intercomparison Project Phase 6 (CMIP-6) of the World Climate Research Programme (WCRP).  
59 Due to observed polar chemical changes caused by energetic particle precipitation (e.g.,  
60 Andersson et al., 2018 and references therein), the solar forcing terms for CMIP-6 now includes

61 medium-high energy electron precipitation (EEP, ~10 keV-1MeV). The recommended EEP  
62 model was developed by Van de Kamp et al. (2016) and uses the geomagnetic index  $A_p$  as a  
63 proxy to describe the variations of precipitating electron flux. The choice of  $A_p$  was more due to  
64 practicality rather than a carefully thought-out scientific decision, as techniques have been  
65 developed to extend the  $A_p$  index beyond its start date in 1932, and thus facilitate long time  
66 series analysis of climate model results to include periods from as early as 1850 (Matthes et al.,  
67 2017). That timing was a requirement for model development to represent solar forcing inside  
68 this effort. Typically, for multi-year coupled-climate model runs  $A_p$  is provided as a daily mean  
69 value rather than its fundamental 3-hour time resolution.

70 However, other geomagnetic indices and solar wind parameters have been used as  
71 proxies to describe radiation belt flux variability. It is well known that the geomagnetic AE index  
72 can be used as a good proxy for substorm activity (e.g., Belakhovsky et al., 2023), and substorms  
73 are expected to trigger processes which lead to high EEP fluxes (Cresswell-Moorcock et al.,  
74 2013; Jaynes et al., 2015; Rodger et al., 2022). Nesse Tyssøy et al. (2021) combined the Medium  
75 Energy Proton and Electron Detectors (MEPED) instrument on board the NOAA/Polar Orbiting  
76 Environmental Satellites (POES) 0° and 90° telescope electron flux measurements, i.e., the  
77 bounce-loss-cone (BLC) and quasi-trapped viewing directions and calculated daily mean values  
78 of electron precipitation fluxes. They concluded that there was a strong correlation between the  
79 daily resolved AE index and >43 keV electron precipitation fluxes. However, in that study AE  
80 was found to be a poor predictor for >292 keV electron fluxes. In contrast, Rodger et al. (2022)  
81 investigated how EEP varied during and after clusters of substorms, looking at the  
82 MEPED/POES 0° (BLC) telescope electron flux measurements. Rodger et al. undertook a  
83 superposed epoch analysis of 15 min resolution median EEP fluxes from 2005-2018 using a  
84 SOPHIE-generated substorm list (Forsyth et al., 2015). During and after substorm clusters there  
85 was a good correlation with AE magnitude for >30keV and >300keV electron fluxes, but only  
86 after careful consideration of the instrument noise-floor.

87 Current substorm mechanisms such as those described in Jaynes et al. (2015) suggest that  
88 VLF chorus waves play a significant role in electron precipitation characteristics, particularly as  
89 electrons drift towards the morning side after injection into the region of MLT midnight. The  
90 geomagnetic index  $K_p$  is often used as a proxy for VLF chorus variability, particularly lower  
91 band chorus (Agapitov et al., 2015; Shprits et al., 2007). Simms et al. (2018) analysed the  
92 variations of trapped relativistic electron fluxes at geostationary orbit, concluding that ULF and  
93 VLF waves (particularly VLF chorus) were important factors in determining variability, and that  
94 solar wind inputs such as velocity, density, and orientation ( $B_z$ ) had moderate influence as well.

95 In order to investigate the suitability of a range of geomagnetic indices and solar wind  
96 parameters to describe the variability of EEP, in this paper we undertake analysis of EEP  
97 measurements from three different satellites. This includes 2 separate spacecraft as well as a  
98 constellation made up of multiple near identical spacecraft. Inter-comparison between the  
99 somewhat disparate satellite observations is made within specific orbital confines where detector  
100 performances are similar, and over common energy ranges. Standard deviations between the  
101 observed electron precipitation fluxes and a range of geomagnetic and solar wind parameters are  
102 determined. Standard errors of those deviations are also calculated, providing a measure of the  
103 uncertainty in the results. From this analysis recommendations are made regarding the best  
104 parameter to use to capture the variability of EEP magnitudes.

## 106 2 Experimental Method

107 Comprehensive descriptions of EEP, in terms of flux measured over a range of energies,  
108 are complicated by the limitations of individual satellite measurements. The Detection of  
109 Electromagnetic Emissions Transmitted from Earthquake Regions (DEMETER) satellite carried  
110 one electron particle detector, but with high energy resolution from 70 keV – 2.2 MeV (Sauvaud  
111 et al., 2006). MEPED/POES EEP measurements (Evans and Greer, 2006) have been made over a  
112 20+ year period and have multiple detectors flying at any one time (Rodger et al., 2010a, 2010b;  
113 Rodger et al., 2022). However, MEPED/POES EEP measurements are limited to three medium  
114 energy integral channels (30 keV – 2.5 MeV), with a potential fourth ( $> 700$  keV) being included  
115 through the contamination of one of the proton channels (Yando et al., 2011; Peck et al., 2015).  
116 The Solar Anomalous and Magnetospheric Particle Explorer (SAMPEX) satellite carried one  
117 detector, designed to be sensitive to relativistic ( $> 1.05$  MeV) electron fluxes (Klecker et al.,  
118 1993; Nakamura et al., 1998). The three satellites measurements of energetic electron fluxes  
119 relevant to this study are detailed below.

### 120 2.1 DEMETER

121 DEMETER was launched into a Sun-synchronous orbit at  $\sim 710$  km in June 2004. The  
122 mission ended in March 2011. DEMETER's Instrument for Detecting Particles (IDP) instrument  
123 measured mostly drift-loss-cone electrons from  $\sim 70$  keV to  $\sim 2.2$  MeV in 126 channels (although  
124 the upper and lower energy channels are not used). The instrument has been described in detail  
125 by Sauvaud et al. (2006). Our study uses IDP data from August 2004 to March 2011. For  
126 operational reasons the IDP instrument measurements were not routinely undertaken at latitudes  
127  $> 65^\circ$  (Cussac et al., 2006), and thus there is a limited range of observations which can be used in  
128 our study. This limitation is discussed in more detail in subsection 2.4. The IDP instrument is  
129 capable of measuring BLC fluxes instead of DLC fluxes when the DEMETER satellite is  
130 overhead of the North Atlantic region (see discussions below). The time resolution of the flux  
131 measurements was 4 s.

### 132 2.2 POES

133 The POES satellites operate in a Sun-synchronous orbit at  $\sim 835$  km. Our study includes  
134 both the NOAA POES satellites (NOAA-15 to NOAA-19), and the EUMetSat POES satellites  
135 (MetOp-1, and -2), all of which carry the SEM-2 instrument suite (Evans and Greer, 2006;  
136 [https://www.ncei.noaa.gov/data/poes-metop-space-environment-  
137 monitor/doc//sem2\\_docs/2006/SEM2v2.0.pdf](https://www.ncei.noaa.gov/data/poes-metop-space-environment-monitor/doc//sem2_docs/2006/SEM2v2.0.pdf)). While suffering from numerous limitations, the  
138 POES SEM-2 MEPED measurements are long lasting, having started in 1998 and continuing to  
139 the present day. POES SEM-2 MEPED has a  $90^\circ$  directed telescope which sees a pitch angle  
140 range much like the DEMETER IDP instrument, and thus can be used to measure BLC fluxes  
141 when the satellite is overhead of the North Atlantic region. POES also has a  $0^\circ$  (BLC) telescope  
142 which is capable of measuring electron precipitation fluxes over a large range of longitudes, and  
143 latitudes (e.g., Rodger et al., 2010b). Corrections for low energy proton contamination are  
144 included in the preparation of the calibrated POES SEM-2 flux data taking into account the  
145 geometric factors of the detectors (Rodger et al., 2010a; Yando et al., 2011). A discussion of  
146 independent evidence that the  $0^\circ$  fluxes are representative of EEP and not dominated by  
147 contamination can be found in Rodger et al. (2022). For the current study we use observations  
148 from 1998 to 2020. The time resolution of the flux measurements was 2 s.

149

150 

## 2.3 SAMPEX

151 SAMPEX made electron flux measurements using the Heavy Ion Large Telescope  
152 (HILT) instrument (Klecker et al., 1993; Nakamura et al., 1998). The satellite orbit was  $520 \times$   
153  $670$  km altitude, with a  $82^\circ$  inclination, and an orbital period of  $\approx 96$  min (Baker et al., 2012). The  
154 HILT measured radiation belt electrons fluxes  $>1.05$  MeV. SAMPEX's HILT instrument was  
155 positioned to measure primarily DLC electron fluxes, similar to the DEMETER IDP instrument  
156 or the POES SEM-2 MEPED  $90^\circ$  telescope. This is discussed more in Dietrich et al. (2010), and  
157 Douma et al. (2017, 2019). For the current study we used observations from August 1996 to  
158 August 2007 (i.e., the non-spin mode period). The time resolution of the HILT flux  
159 measurements was 0.1 s.

160

161 

## 2.4 Location of Bounce-Loss-cone measurements

162 The pitch angle populations measured by any given satellite particle detector is dependent  
163 on the orientation of the detector to the local magnetic field line. Thus, the populations vary  
164 substantially as the satellite moves along its orbit. Figure 1 is a three-panel plot of the radiation  
165 belt populations observed by the DEMETER, POES, SAMPEX particle detectors, respectively  
166 throughout their low altitude orbits. In this figure the location on the map is the projection along  
167 the satellite field line to 100 km altitude, using the IGRF 2005 model (Macmillan and Maus,  
168 2005). The colour scale represents 6 different particle populations, ranging from viewing all of  
169 the trapped and precipitating fluxes (All), to only those precipitating fluxes (FL BLC only).  
170 These categories are described in detail in Rodger et al. (2010b), and Whittaker et al. (2013). On  
171 each panel a green rectangle indicates the region in which the satellite detector views only  
172 precipitating fluxes. Typically, this region is located in the north of the Atlantic Ocean region,  
173 typically from  $30^\circ\text{N}$  to  $60^\circ\text{deg N}$ , and  $60^\circ\text{W}$  to  $30^\circ\text{E}$ . In the upper panel there are no flux  
174 measurements to the west at high latitude, as the DEMETER instrument was not operating in this  
175 region. In the middle panel a smaller rectangle is used for the POES  $90^\circ$  particle detector in order  
176 to remove the influence of Drift-Loss-Cone measurements to the western side of the box, as  
177 shown by the green dashed area. For POES and SAMPEX there are some high latitude regions  
178 where the IGRF magnetic field model returned an 'open' field line result, and these areas are  
179 denoted by a very dark blue 'Fail' category.

180 In addition to BLC measurements made in the North Atlantic we also make use of the  
181 MEPED/POES  $0^\circ$  directed telescope, as it is capable of measuring electron precipitation over all  
182 longitudes at the range of mid-latitudes under study here. We use this capability to make  
183 comparisons with the conclusions determined by the regionally restricted North Atlantic  
184 observations. The equivalent radiation belt populations observed by the  $0^\circ$  directed telescopes  
185 are shown in Figure A3 of Rodger et al. (2010b).

186 

## 2.5 Scatter factor

187 The main goal of our study is examine the variability in electron precipitation fluxes  
188 when binned by  $L$ -shell and a range of different activity indices, such that we can investigate  
189 what indices can best be used to capture the relationships, i.e., a good quality (low scatter)

190 relationship between precipitation magnitude, geomagnetic latitude, and activity driver. In order  
 191 to account for the scatter in a given relationship, we determine the typical ‘scatter factor’ for  
 192 each satellite detector discussed, within the measurement region denoted by the rectangles shown  
 193 in Figure 1.

194 The scatter factor is the geometric mean of the standard deviations of the all the flux data  
 195 within a measurement bin, given by an  $L$ -shell versus activity index grid, e.g.,  $0.25 L \times 5 \text{ nT}$  of  
 196  $A_p$ . We require each bin to have at least five data points. The standard deviation of all the flux  
 197 values is found within each bin, and the process is repeated for all bins. Finally, the geometric  
 198 (logarithmic) mean of all the standard deviations is calculated. A lower scatter factor indicates a  
 199 lower overall set of standard deviations. Thus, the geomagnetic index or solar wind parameter  
 200 with the lowest scatter should be a reliable way to predict which is the “best” proxy to link EEP  
 201 magnitude in an  $L$  versus index/proxy relationship.

202

### 203 **3 Calculation of the DEMETER noise floor**

204 Of the three satellite particle detector instruments, the DEMETER IDP has the highest  
 205 energy resolution capabilities, but historically there has been less focus on understanding the  
 206 sensitivity limits of the IDP instrument than for the POES SEM-2 and SAMPEX HILT  
 207 instruments. We therefore undertake an analysis of the DEMETER IDP noise floor, and how it  
 208 varies with energy, as presented in this section.

209 Inspection of individual energy spectra in the DEMETER IDP data often show that the  
 210 fluxes reported for energy bins above 800 keV are larger than those for lower energy bins. Even  
 211 during very quiet geomagnetic times this relationship is observable e.g., Figure 4 in Whittaker et  
 212 al. (2013), and over many  $L$ -shell ranges. The fundamental cause of this energy dependent  
 213 behaviour is due to the energy-dependent variation of the IDP instrument geometric factor  
 214 (Sauvaud et al., 2006). An example of the variation of IDP fluxes with energy is presented in  
 215 Figure 2. Measurements from a half orbit on 6 May 2006 are shown, with coloured lines  
 216 representing the energy dependent fluxes for a range of 0.25  $L$ -shell bins during this half-orbit.  
 217 There are noticeable increases in IDP reported flux at higher energies ( $>800 \text{ keV}$ ) for some  $L$ -  
 218 shell ranges.

219 Electron fluxes are computed by dividing the measured count rate in each energy bin by  
 220 the energy geometry factor  $G(E)$ , which is described in Sauvaud et al. (Figure 7, 2006), with  
 221 units of  $\text{cm}^2\text{sr}$ . The IDP used a routine sampling mode with a  $0.25 \text{ s}^{-1}$  count rate. The spacing  
 222 between the differential energy channels in routine mode is 17.8 keV, which gives a non-zero  
 223 differential count rate minimum value of  $0.014 \text{ el. s}^{-1}\text{keV}^{-1}$  (i.e., 1 count per 4 s in a 17.8 keV bin  
 224 produces a minimum value of  $1/(4 \times 17.8)$ ). When divided by  $G(E)$ , this defines the instrument  
 225 noise floor flux levels as exhibited in Figure 2. In addition, inspection of the fluxes close to the  
 226 noise floor shows quantisation of the values. This is especially visible in the low energy/low flux  
 227 regime in Figure 2 where we can see, for example, values of  $1 \times 10^{-2}$  or  $2 \times 10^{-2}$  or  $3 \times 10^{-2} \text{ el.}$   
 228  $\text{cm}^{-2}\text{s}^{-1}\text{sr}^{-1}\text{keV}^{-1}$  without values in between - this quantisation suggests that flux values just above  
 229 the IDP instrument noise floor are still not accurate, due to the quantisation limits of the different  
 230 count rate values for 1, 2, or 3 counts per time and energy range. A solid black line has been

231 added to Figure 2 in order to indicate the flux levels below which quantisation appears to be an  
232 issue.

233 In order to take into account the uncertainty of the values close to the instrument noise  
234 floor, we identify an effective noise floor which ignores flux values that are inherently unreliable  
235 due to the impacts of quantisation as well as the minimum noise floor. Figure 3 reproduces the  
236 DEMETER IDP electron flux data from the half orbit on 6 May 2006 shown in Figure 2, where  
237 unreliable electron flux values have been removed. The effective noise floor is shown as a black  
238 line and can be thought of as flux values corresponding to a level of 2 counts/s in each energy  
239 bin (i.e., 8 counts in a 0.25 s sampling period), converted to flux using the instrument geometry  
240 factor. In our analysis electron flux values that are unlikely to be meaningful measures of flux  
241 are discarded using this effective noise floor.

242 For the POES SEM-2 detector the effective noise floor has previously shown to be at 1  
243 count/s (Rodger et al., 2010a; Yando et al., 2011). In this study the noise floor is not a significant  
244 issue for SAMPEX HILT due to the very large geometric factor detector, which was designed to  
245 provide accurate flux measurements even at 20 ms sampling (Klecker et al., 1993).

246

## 247 **4 Results**

248 In this section two energy ranges are considered: medium energy (section 4.1) and high  
249 energy (section 4.2). Here, medium energy precipitation is investigated using integral >90 keV or  
250 >100 keV electron precipitation fluxes – depending on the detector. For the DEMETER data all  
251 of the IDP 124 differential energy channels were combined to give an integral flux value  
252 >90 keV, while for POES the >100 keV integral channel was used as a comparison. Both  
253 detectors measure energies up to about >2 MeV. For the high energy analysis only the  
254 DEMETER energy channels >700 keV were combined to give an integral value. The POES E4  
255 >700 keV channel was used as a comparison, as well as the >1.05 MeV SAMPEX HILT data.

256 Four geomagnetic activity indices are considered in terms of their link to electron  
257 precipitation at this energy, i.e.,  $A_p$ ,  $K_p$ ,  $Dst$ , and  $AE$ .  $A_p$  and  $K_p$  have a fundamental time  
258 resolution of 3 hours, while  $Dst$  and  $AE$  have hourly resolution. Three solar wind indices are also  
259 considered, i.e., solar wind velocity ( $V_x$ ), southward interplanetary magnetic field ( $B_z$ ), and the  
260 solar wind dynamic pressure ( $P_{dyn}$ ). The solar wind data have 1 minute time resolution and are  
261 expressed in GSM coordinates.

262 The electron precipitation flux measurements sampled within each 0.25  $L$ -shell section of  
263 the orbital path through the region sampled. Typically, the time taken for the satellites to fly  
264 through a 0.25  $L$  wide section at  $L \sim 4$  or so is in the order of 1 minute, so many flux  
265 measurements were combined for each section, depending on the instrument sampling rate. Each  
266 average flux value was then associated with the geomagnetic and solar wind index parameters at  
267 the average time of the measurements. Since the indices are recorded with 3-hourly, hourly or  
268 minute resolution we used linear interpolation to infer an index value to coincide with the time  
269 that the average flux was recorded. This interpolation was done with all of the geomagnetic  
270 indices and solar wind parameters. Once flux/index pairs were calculated for each 0.25  $L$ -shell

271 section in each orbit through the region of interest they can be binned by activity level. An  
 272 analysis of the scatter factors per activity bin can then be made. The subsections below describe  
 273 such analysis for the medium and high energy fluxes.

#### 274 **4.1 Electron precipitation >90 keV**

275 The bounce-loss-cone binned electron precipitation fluxes from the DEMETER IDP  
 276 instrument are shown in Figure 4, determined from within the North Atlantic sample region  
 277 shown in Figure 1. The four panels show the results for AE, Kp, Dst, and Ap geomagnetic  
 278 indices respectively, with the colour scale representing the logarithm of the mean flux in each  
 279 bin. White colours indicate bins with no data, while coloured areas with white dots indicate bins  
 280 where the flux magnitude was comparable to the standard deviation, i.e., high variability within  
 281 the bin. These conditions typically occur where precipitation fluxes are very low. Black lines  
 282 represent the L-shell of the plasmopause as a function of each geomagnetic index using the  
 283 formulations given by O'Brien and Moldwin (2003). We note that O'Brien and Moldwin do not  
 284 provide a plasmopause model for Ap, hence the lack of a black line in this panel.

285 In each panel of Figure 4 the occurrence of the largest fluxes is concentrated towards the  
 286 highest geomagnetic activity levels, and towards the highest range of the *L*-shell bins. There is  
 287 some overlap with high precipitating fluxes and the location of the plasmopause, although  
 288 DEMETER rarely sampled at *L*-shells high enough to investigate locations outside the  
 289 plasmopause. There is an indication of precipitating fluxes moving to lower *L* for increasing  
 290 geomagnetic activity, consistent with the plasmopause moving inwards towards low *L*-shells  
 291 (Carpenter and Anderson, 1992). The Dst panel in particular shows a tendency for the flux  
 292 pattern to follow the behaviour of the plasmopause, with flux levels dropping by approximately  
 293 two orders of magnitude within 1.5 *L* (6 bins) inside of the plasmopause at all geomagnetic  
 294 activity levels. Very low values of the >90 keV flux were seen below *L*=2.5 for the majority of  
 295 geomagnetic conditions.

296 POES >100 keV precipitation fluxes in the North Atlantic sample region are shown in  
 297 Figure 5. The panels are the same format as shown in Figure 4, except that they extend to more  
 298 disturbed geomagnetic conditions. As the POES SEM-2 dataset is very long-lasting, it spans a  
 299 wider range of disturbed conditions. Additionally, each bin has fluxes that are high enough that  
 300 they are larger than the standard deviation in the bin and thus no white dots appear. This also true  
 301 for Figures 6 and 9 shown later in the manuscript. The fluxes shown in Figure 5 are based on the  
 302 POES 90° detector viewing the BLC in the sample region shown in Figure 1. The panels contain  
 303 flux values up to slightly higher *L*-shells than was visible in the equivalent DEMETER panels,  
 304 and thus give a somewhat more complete picture of the variations of flux at *L*-shells higher than  
 305 the plasmopause. Both satellite datasets show flux values of  $\sim 10^4$  el.cm<sup>-2</sup>s<sup>-1</sup>sr<sup>-1</sup> in the vicinity of  
 306 the plasmopause. However, the POES >100 keV precipitating fluxes are clearly larger outside  
 307 the plasmopause when contrasted with near the plasmopause. As with the DEMETER panels,  
 308 larger electron precipitation fluxes occur during higher geomagnetic activity levels, but more  
 309 detailed analysis is needed to discern which index provides a better correlation with the fluxes.  
 310 This will be investigated in detail at the end of this subsection.

311 DEMETER IDP and the POES SEM-2 90° telescope only views the BLC in the North  
 312 Atlantic region, allowing direct comparisons of these measurements in that sampling region.



313 However, it is possible to use the SEM-2 0° telescope on POES to study the BLC precipitation  
 314 electron fluxes over all longitudes to provide another comparison. Figure 6 shows the >100 keV  
 315 integral electron precipitation fluxes from the SEM-2 0° telescope using all longitudes, and also  
 316 investigating higher  $L$ -shells as that is possible for this dataset. The figure is otherwise in the  
 317 same format as Figures 4 and 5. The main differences between the global 0° POES data plot  
 318 (Figure 6) compared with the North Atlantic 90° POES data plot (Figure 5) is that the panels  
 319 include a wider range of geomagnetic activity and  $L$ -shell – this is caused by the larger dataset  
 320 available when using measurements made spanning all longitudes (i.e., the 0° POES data).  
 321 Additionally, the slightly restrictive North Atlantic upper latitude limit for POES 90° precipitating  
 322 flux (shown in Figure 1) reduces the 90-deg observations for  $L > 5$ . However, where the two plots  
 323 overlap in geomagnetic activity and  $L$ -shell both figures agree regarding flux distributions  
 324 peaking in the vicinity of the plasmapause. As in the previous figures, the electron precipitation  
 325 fluxes are larger at  $L$ -shells outside of the plasmapause, and larger for more disturbed  
 326 geomagnetic conditions. However, precipitating flux values are seen to decrease at the highest  $L$ -  
 327 shells. This is because as the influence of radiation-belt precipitation loss processes tends to  
 328 become less dominant (e.g., section 3 of Ripoll et al., 2020). It is likely that at the very highest  
 329 geomagnetic activity levels the fluxes are dominated by substorm-induced electron precipitation,  
 330 resulting in a wider  $L$ -shell spread and higher fluxes, than seen for less active conditions. This  
 331 suggestion is supported by the earlier work of Cresswell-Moorcock et al. (2013) and Rodger et  
 332 al. (2022), who both used superposed epoch analysis of POES measurements to show evidence  
 333 of electron precipitation from substorms extending beyond  $L > 10$ .

334 In order to compare the three measurement scenarios illustrated above, scatter factor  
 335 analysis as described in section 2.5 was undertaken. The results of this analysis is presented in  
 336 Table 1. Geometric mean standard deviations (STD) are shown along with their standard error  
 337 (SE) where  $SE = STD/\sqrt{\text{number of samples}}$ . Summary details for each of the three satellite-  
 338 measurement scenarios are given at the top of the columns. The indices under investigation are  
 339 grouped into two categories: Geomagnetic, and Solar Wind/IMF (Interplanetary Magnetic  
 340 Field),. The solar wind /IMF parameters are the  $x$ -component of solar wind velocity ( $V_x$ ), the  
 341 magnetic field  $z$ -component ( $B_z$ ), and the solar wind dynamic pressure ( $P_{dyn}$ ), all expressed in  
 342 GSM coordinates.

343 In Table 1 the parameter with the smallest scatter factor for each satellite dataset is  
 344 highlighted in **bold and underlined**. The next best scatter factor is indicated through *italics with*  
 345 *underlining*. This highlighting has been undertaken separately for the fundamental time  
 346 resolution of each index. The  $A_p$  and  $Dst$  indices consistently generate the lowest scatter factors  
 347 in all three datasets. As is visually apparent from Figures 4 to 6 the DEMETER dataset has  
 348 higher scatter values for each individual index when compared with the equivalent POES  
 349 datasets. In Table 1, none of the solar wind/IMF parameters result in scatter factors that occur in  
 350 the two smallest scatter factors, i.e., the two best indices.

351 The standard errors shown in Table 1 provide an indication of the uncertainty in the  
 352 scatter factor values. As an example, for the POES >100 keV 90° detector (middle) column the  
 353  $Dst$  and  $A_p$  indices have scatter factors of  $2.3 \pm 0.1$  and  $2.5 \pm 0.1$ . The error associated with these  
 354 scatter factor values is substantially smaller than the difference between the two top indices and  
 355 the next best values ( $3.6 \pm 0.2$  for  $K_p$ ). This is true for  $A_p$  and  $Dst$  in the POES worldwide dataset  
 356 (right hand column) and for  $Dst$  in the DEMETER (left hand) column. For DEMETER the

357 standard errors in the scatter factors for Ap, Kp, and AE are such that there is no clear distinction  
 358 between them, and so no index has been highlighted as the next best scatter factor, i.e., no  
 359 parameter is underlined and in italics.

360

361 **Table 1:** The scatter factors for medium energy electron precipitation derived from the standard  
 362 deviations of three precipitating electron flux datasets when binned by L-shell and activity index.  
 363 Indices are separated into Geomagnetic and Solar Wind parameters. The activity parameter with  
 364 the smallest (i.e., best) scatter factor is highlighted in **bold and underlined**, while the next best  
 365 result is indicated through *italics with underlining*. The standard error of each scatter factor is  
 366 shown as a  $\pm$  value. See text for more details.

367

	DEMETER >90 keV	POES >100 keV	POES >100 keV
	IDP	90° detector	0° detector
	North Atlantic	North Atlantic	Worldwide
	$1.5 < L < 4.5$	$1.5 < L < 5.5$	$1.5 < L < 7$
	Scatter factor $\times 10^{-2}$ ( $\text{cm}^{-2}\text{s}^{-1}\text{sr}^{-1}$ )	Scatter factor $\times 10^{-3}$ ( $\text{cm}^{-2}\text{s}^{-1}\text{sr}^{-1}$ )	Scatter factor $\times 10^{-3}$ ( $\text{cm}^{-2}\text{s}^{-1}\text{sr}^{-1}$ )
<b>INDEX</b>			
<b><i>Geomagnetic</i></b>			
Ap (3 hours)	$11.4 \pm 0.7$	<u><i><math>2.5 \pm 0.1</math></i></u>	<b><u><math>3.4 \pm 0.1</math></u></b>
Dst (1 hour)	<b><u><math>9.7 \pm 0.5</math></u></b>	<u><i><math>2.3 \pm 0.1</math></i></u>	<u><i><math>4.3 \pm 0.2</math></i></u>
Kp (3 hours)	$11.6 \pm 0.6$	$3.6 \pm 0.2$	$4.8 \pm 0.2$
AE (1 hour)	$11.9 \pm 0.6$	$3.8 \pm 0.2$	$5.9 \pm 0.1$
<b><i>Solar Wind/IMF</i></b>			
$V_x$ (1 minute)	$20.9 \pm 1.1$	$3.9 \pm 0.2$	$5.5 \pm 0.2$
$B_z$ (1 minute)	$26.2 \pm 1.4$	$6.1 \pm 0.3$	$10.3 \pm 0.6$
$P_{dyn}$ (1 minute)	$21.3 \pm 1.1$	$6.2 \pm 0.3$	$8.9 \pm 0.4$

368

369 The indices analysed in Table 1 have a wide range of time resolutions, from 1 minute to 3 hours.  
 370 However, the index values are determined at the time of each flux measurement. In order to test  
 371 for potential delay times between the most active periods and electron precipitation flux  
 372 variations the analysis was repeated, testing for the maximum disturbance value (either a  
 373 maximum or minimum value depending on the parameter) in the 24 hours prior to the flux  
 374 measurement. This is consistent with the normal definition of Ap\* (Allen and Wilkinson, 1993)  
 375 which has been used as a measure of a geomagnetic storm peak intensity. The scatter factors for  
 376 medium electron precipitation energies using maximum 24-hour disturbance indices are  
 377 presented in Supplementary Information Table S1. Coloured fonts are used to indicate whether  
 378 the scatter factor for any particular index has increased or decreased compared with the values

379 shown in Table 1, e.g., the scatter factor for the DEMETER fluxes increases from 11.4 ( $A_p$ ) to  
380 13.8 ( $A_p^*$ ) when the index is analysed over 24 hours, as denoted by a red font. Blue fonts  
381 indicate a reduction in scatter factor over 24-hour timescales suggesting a smaller standard  
382 deviation between the fluxes and the 24-hour index. Generally, the best and second-best  
383 parameters remain  $A_p^*$  and  $Dst^*$  as good proxies for medium energy electron precipitation  
384 despite the different method used in index value selection.

#### 385 **4.2 Electron precipitation >700 keV**

386 In this section the analysis techniques of the previous section is repeated, but for  
387 higher energy electron precipitation fluxes (i.e., >700 keV) rather than for medium energies. As  
388 DEMETER IDP has 126 differential energy channels it is possible to combine the highest energy  
389 channels and produce an integral flux > 700 keV. Figure 7 shows results of plotting  $L$ -shell  
390 versus geomagnetic indices AE,  $K_p$ ,  $Dst$  and  $A_p$  in the same format as Figure 4 but for the high  
391 energy electron precipitation measured by DEMETER in the North Atlantic sample region. In  
392 this energy range the data tend to be sparse as few DEMETER measurements have integrated  
393 flux values higher than the effective noise floor. However, as before, high fluxes are observed  
394 when the index of activity increases. Note that the flux colour-scale maxima are significantly  
395 lower than the equivalent panels in Figure 4.

396 Further analysis of high energy electron precipitation is provided by SAMPEX HILT  
397 measurements in the North Atlantic sampling region, where the detector is measuring fluxes  
398 within the BLC. Figure 8 shows the SAMPEX data plotted in the same format as Figure 7. High  
399 energy fluxes tend to be larger at more disturbed levels of geomagnetic disturbance and  
400 associated with regions just outside of the plasmopause; clearly, this is consistent with previous  
401 figures. Figure 8 covers the  $L$ -activity space much more comprehensively than Figure 7. A very  
402 significant factor in this is lack of DEMETER coverage above  $65^\circ$  latitude, which limits  $L$ -shell  
403 range of Figure 7 (DEMETER) relative to Figure 8 (SAMPEX). DEMETER collected data for  
404 ~6.5 years in comparison to SAMPEX's 11 years of non-spin period observations. In addition,  
405 the DEMETER operational period was also much geomagnetically quieter than SAMPEX  
406 sampled, with significant time periods where the radiation belts had largely faded away (Rodger  
407 et al., 2016).

408 As a final comparison, the POES SEM-2 E4 >700 keV  $0^\circ$  detector is used to provide a  
409 measure of high energy electron precipitation flux over all longitudes. Figure 9 shows the POES  
410 > 700 keV electron precipitation fluxes in the same format as the SAMPEX data shown in Figure  
411 8. Note that although the  $L$ -shell range is the same as in Figure 8, the geomagnetic index ranges  
412 are quite different. This is a result of examining the 22+ years of POES data, leading to a larger  
413 range of geomagnetic disturbance level, compared with the 11 years of SAMPEX data analysed.  
414 The distributions in Figure 9 (POES E4 >700 keV  $0^\circ$ , all longitudes) look different from the  
415 distributions in Figure 8 (SAMPEX >1.04 MeV, North Atlantic) because of the wider range of  
416 geomagnetic activity incorporated in the more extensive POES  $0^\circ$  dataset. For example, the  $Dst$   
417 panel in Figure 8 shows a lowest value of -120 nT while in Figure 9  $Dst$  goes down to -275 nT.  
418 Where the two panels overlap in geomagnetic activity and  $L$ -shell there are similar flux  
419 distributions. This is also seen in the other comparable panels for Figure 8 and 9. Although there  
420 is some visual correspondence of enhanced flux in the vicinity of the plasmopause location, the  
421 panels of Figure 9 are dominated by high flux, wide  $L$ -shell range features, at the highest

422 magnetic disturbance levels. A comparison between POES 0° >100 keV (Figure 6) and >700  
423 keV precipitation fluxes (Figure 9) shows more banded structure at the higher energies than the  
424 lower ones. These features are possibly due to substorm-induced precipitation, or possibly  
425 electro-magnetic ion-cyclotron (EMIC) wave-induced precipitation (e.g., Cresswell Morecock et  
426 al., 2013; Usanova et al., 2014). In Figure 9 the Kp panel's high activity, high flux distributions  
427 are much smoother, and do not show such banded structure, which is most likely due to the Kp  
428 index parameter resolution.

429 Scatter factor analysis of high energy electron precipitation (>700 keV) for the three  
430 measurement scenarios is given in Table 2. This table is the same format as Table 1, although  
431 now including datasets from DEMETER, POES and SAMPEX. The two indices giving the  
432 lowest scatter values, i.e., best, are highlighted as before. Here Kp is identified as the index with  
433 the least scatter over a range of scenarios, with AE the next best. Notably there is a range of  
434 contenders coming from the DEMETER measurements, with Ap the best at original time  
435 resolutions. Also notably, one of the solar wind/IMF parameters features in the 'best'  
436 highlighting, with  $V_x$  a close second for POES >700 keV measurements. Taking into account the  
437 standard error values for each scatter factor suggests that some of the solar wind parameters are  
438 potentially as good a proxy for >700 keV electron precipitation flux as the geomagnetic indices.  
439 Table S2 in Supplementary Information shows the scatter factors for the maximum disturbance  
440 value (either a maximum or minimum value depending on the parameter) in the 24 hours prior to  
441 the flux measurement. This tests for potential delay times between the most active periods and  
442 electron precipitation flux variations. Generally, the best and second best parameters remain Kp  
443 and AE as good proxies for high energy electron precipitation despite the different method used  
444 in index value selection.

445 **Table 2:** The scatter factors for high energy (>700 keV) electron precipitation derived from the  
446 standard deviations of three electron flux measurement scenarios when binned by  $L$ -shell and  
447 index of activity. The activity parameter with the smallest (best) scatter factor is highlighted in  
448 **bold and underlined**, while the next best result is indicated through *italics with underlining*. The  
449 standard error of each scatter factor is shown as a  $\pm$  value. Format is the same as Table 1. See  
450 text for more details.

	DEMETER >700 keV	POES >700 keV	SAMPEX >1.05 MeV
	IDP	P6 0° detector	HILT
	North Atlantic	Worldwide	North Atlantic
	$1.5 < L < 4.5$	$1.5 < L < 7$	$1.5 < L < 7.25$
	Scatter factor x $10^{-2}$ ( $\text{cm}^{-2}\text{s}^{-1}\text{sr}^{-1}$ )	Scatter factor x $10^{-3}$ ( $\text{cm}^{-2}\text{s}^{-1}\text{sr}^{-1}$ )	Scatter factor x $10^{-2}$ ( $\text{cm}^{-2}\text{s}^{-1}\text{sr}^{-1}$ )
<b>INDEX</b>			
<b>Geomagnetic</b>			
Ap (3 hours)	<b><u><math>32.6 \pm 1.9</math></u></b>	$11.5 \pm 0.3$	$56.0 \pm 3.5$
Dst (1 hour)	$37.0 \pm 2.0$	$11.0 \pm 0.4$	$56.3 \pm 2.9$
Kp (3 hours)	$34.8 \pm 1.9$	<b><u><math>9.8 \pm 0.5</math></u></b>	<b><u><math>53.3 \pm 2.7</math></u></b>
AE (1 hour)	<b><u><math>33.8 \pm 1.8</math></u></b>	$11.5 \pm 0.3$	<b><u><math>54.8 \pm 1.9</math></u></b>
<b>Solar Wind/IMF</b>			
$V_x$ (1 minute)	$40.6 \pm 2.1$	<b><u><math>10.3 \pm 0.5</math></u></b>	$55.4 \pm 3.0$
$B_z$ (1 minute)	$44.1 \pm 2.3$	$11.7 \pm 0.6$	$60.9 \pm 3.3$
$P_{\text{dyn}}$ (1 minute)	$40.2 \pm 2.1$	$11.5 \pm 0.5$	$59.1 \pm 3.4$

451

452 **5 Discussion**

453 Scatter factor analysis, based on the standard deviation between electron precipitation  
454 flux and geomagnetic indices/solar wind parameters, has been used to determine the most  
455 reliable proxies to empirically capture the variation of electron precipitation. The calculation of  
456 scatter factor was undertaken for a wide range of geomagnetic latitude (given by  $L$ -shell) and  
457 activity level. Tables 1 and 2 summarise the results of the scatter factor analysis for medium  
458 energy electron precipitation (100's of keV) and for high energies ( $\sim 1$  MeV), using several  
459 different satellites/instruments. The scatter factors of the DEMETER IDP >90 keV integrated  
460 measurements are approximately a factor of 30 larger than the POES >100 keV integral  
461 measurements. This is most likely due to instrumental differences, in combination with a bias  
462 towards lower  $L$ -shell for DEMETER measurements. The scatter factors for the SAMPEX HILT  
463 measurements are also larger than the POES ones, most likely due to the large geometric factor  
464 of the HILT instrument. These factors make the inter-comparison of scatter factors between  
465 instruments (i.e., different columns in the tables) very difficult. However, the electron  
466 precipitation flux dataset are the same for each column in the tables. As such, they can be  
467 compared to find the best proxy for each dataset, and inter-dataset comparisons undertaken.

468 . In order to test for potential delay times between the most active periods and electron  
469 precipitation flux variations the analysis was repeated, testing for the maximum disturbance  
470 value (either a maximum or minimum value depending on the parameter) in the 24 hours prior to  
471 the flux measurement. These results are provided in the Supplementary Information Tables S1  
472 and S2. Overall, there was a small reduction in scatter factor using the 24-hour indices (peak  
473 disturbance value), with the most notable change occurring for the solar wind parameters, i.e., -

474 13% for the medium energy results. This can be seen through the preponderance of blue  
475 colouring of the solar wind values in the lower sections of Tables S1 and S2. No clear change  
476 occurred for scatter factors calculated with the 24-hour geomagnetic indices (shown by a mixture  
477 of red and blue fonts). Converting from hourly index values to 24-hour maximum (minimum)  
478 values makes almost no difference to the scatter factors, which suggests that electron  
479 precipitation flux process timescales last hours rather than minutes. Despite the improvement of  
480 the scatter factors for the 24-hour solar wind results, the same ‘best’ proxies for medium and  
481 high energy electron precipitation were identified by both the fundamental time resolution and  
482 24-hour maximum disturbance analysis.

483 Despite using three different low-Earth orbiting satellites, and a range of differing  
484 detector viewing configurations, the scatter factor analysis undertaken in this study shows  
485 consistent identification of the best proxies to empirically represent electron precipitation. For  
486 the medium energy electron precipitation (several tens to hundred’s of keV) the best proxies are  
487 Ap and Dst. For the high energy electron precipitation (~1 MeV) the best proxies are Kp and AE.  
488 These findings are independent of the time resolution of the proxy. While there are different  
489 ranges of geomagnetic activity exhibited by each satellite dataset they consistently identify Dst  
490 and Ap as the top two proxy indices for describing the medium energy precipitation flux  
491 variability, along with Kp and AE for the high energy proxy. This suggests a consistency in the  
492 application of a given energy proxy over a wide range of geomagnetic activity.

493 The identification of Ap and Dst as the best proxies for the medium energy electron  
494 precipitation is consistent with the injection and transport of mid (i.e., seed) and low-energy (i.e.,  
495 source) electrons into the inner magnetosphere which occurs during enhanced solar wind and  
496 geomagnetic activity. Precipitation of mid energy electrons is primarily through processes  
497 dominated by VLF waves, particularly chorus occurring just outside of the plasmopause  
498 (Whittaker et al., 2014; van de Kamp et al., 2016). Ap is a good measure of convection  
499 (Thomsen, 2004) and Dst indicates increased transport (e.g., Zhao and Xi, 2013) consistent with  
500 this chorus-driven precipitation framework.

501 The identification of Kp and AE as the best proxies for high energy electron precipitation  
502 can also be considered within the framework of chorus whistler mode wave drivers of seed  
503 electrons (hundreds of keV electrons) accelerating them to produce relativistic electrons (Jaynes  
504 et al., 2015). Kp is a measure of convection, and AE indicates substorm activity. Convection  
505 associated with substorms will generate intense chorus producing relativistic electron microburst  
506 precipitation (Douma et al., 2017, Douma et al., 2019) and also EMIC waves which also produce  
507 relativistic electron precipitation (Blum et al., 2015; Jaynes et al., 2015; Hendry et al., 2017 and  
508 references therein).

## 509 **6 Conclusions**

510 Empirical models of energetic electron precipitation forcing (EEP) have been made using  
511 geomagnetic indices as proxies. The EEP forcing models need to be suitable for incorporation  
512 into coupled-climate model runs and allow for periods outside the current satellite era to be  
513 included in the climate model runs. In the current study the suitability of a range of proxies to  
514 represent EEP fluxes is investigated, using three different satellite electron precipitation datasets  
515 (DEMETER, POES, and SAMPEX). In order to measure electron precipitation fluxes without

516 the dominating effects of much larger trapped fluxes being incorporated, we primarily focused  
517 on measurements made above the North Atlantic region. This was always the case for  
518 DEMETER and SAMPEX observations, whereas the POES bounce-loss-cone measurements had  
519 the capability of more global analysis.

520 In order to take into account the noise floor of the DEMETER IDP measurements an  
521 estimate of the sensitivity of each highly resolved energy channel was made. The description of  
522 the DEMETER IDP effective noise floor provided a route through which only realistic fluxes  
523 were included in the suitability analysis.

524 The suitability of each proxy to represent EEP fluxes was found using a scatter factor  
525 which summarised the EEP flux variations over a wide  $L$ -shell range (i.e., geomagnetic latitude)  
526 and a wide range of activity levels. The scatter factor for each satellite/proxy combination was  
527 calculated through the geometric mean of the standard deviations of the all the flux data within  
528 each measurement bin given by an  $L$ -shell versus activity index grid. Lower scatter factors are  
529 indicative of a lower overall set of standard deviations, and were used to identify the most  
530 appropriate proxy. A standard error of each scatter factor was calculated and used as an  
531 indication of the uncertainty in the scatter factor results. This analysis was undertaken for four  
532 geomagnetic indices (Ap, Dst, Kp, AE), and for 3 solar wind/IMF parameters ( $V_x$ ,  $B_z$ ,  $P_{dyn}$ ).

533 The scatter factor analysis shows consistent identification of the best proxies for electron  
534 precipitation, even using three different low-Earth orbiting satellite datasets, and a range of  
535 detector viewing configurations. For the medium energy electron precipitation (several tens to  
536 hundred's of keV) the best proxies are Ap and Dst. For the high energy electron precipitation (~1  
537 MeV) the best proxies are Kp and AE.

538 The identification of the Ap index as the best proxy for medium energy EEP is a  
539 vindication of the approach taken by van de Kamp et al. (2016) to provide an EEP forcing  
540 capability in Matthes et al. (2017). The van de Kamp flux model described EEP fluxes over a  
541 range of 10 keV to 1 MeV. The results found here suggest that while Ap is a good proxy for  
542 most of that energy range, it is likely that for electron energies >700 keV an index more  
543 associated with substorm activity (such as AE) would be more appropriate.

## 544 **Acknowledgments**

545 The authors wish to thank the personnel who developed, maintain, and operate the NOAA/POES  
546 spacecraft and also those who supported the earlier DEMETER and SAMPEX satellites.

547

## 548 **Open Research**

549 The data used in this paper are available at the CNES/CESR Centre de Donnees pour la Physique  
550 des Plasmas (CDPP - Demeter IDP, <https://cdpp-archive.cnes.fr/user/cdpp/modules/1723>) and

551 NOAA's National Geophysical Data Center (NGDC - POES MEPED data,  
552 <https://ngdc.noaa.gov/stp/satellite/poes/>). Data availability for SAMPEX is described at  
553 <http://www.srl.caltech.edu/sampex/DataCenter/index.html>. The Solar Wind parameters were  
554 obtained from <https://solarscience.msfc.nasa.gov/SolarWind.shtml>. Accessed: 2021-05-25.  
555 AE, Ap, Dst, and Kp geomagnetic activity indices were downloaded from the UK Solar System  
556 Data Centre (<https://www.ukssdc.ac.uk/>). Dynamic pressure (P<sub>dyn</sub>), solar wind velocity (V<sub>x</sub>),  
557 and interplanetary magnetic field (B<sub>z</sub>) data were obtained from the SuperMAG website  
558 (<https://supermag.jhuapl.edu/>); for the use of these parameters we gratefully acknowledge the  
559 SuperMAG collaborators (<https://supermag.jhuapl.edu/info/?page=acknowledgement>)

560

## 561 **References**

562 Agapitov, O. V., Artemyev, A. V., Mourenas, D., Mozer, F. S., & Krasnoselskikh, V. (2015).  
563 Empirical model of lower band chorus wave distribution in the outer radiation belt. *Journal of*  
564 *Geophysical Research: Space Physics*, 120, 10425–10442. <https://doi.org/10.1002/2015JA02182>

565

566 Allen, J. H., & Wilkinson, D. C. (1993). Solar-Terrestrial Activity Affecting Systems in Space  
567 and on Earth. In “Solar-Terrestrial Predictions-IV: Proceedings of a  
568 Workshop at Ottawa, Canada May 18-22, 1992”, Edited by J. Hruska, M.A. Shea, D.F.  
569 Smart, and G. Heckman. 75-107, National Oceanic and Atmospheric Administration,  
570 Environmental Research Laboratories, Boulder, Colorado.

571

572 Andersson, M. E., Verronen, P. T., Marsh, D. R., Seppälä, A., Päivärinta, S.-M., Rodger, C. J., et  
573 al., (2018). Polar ozone response to energetic particle precipitation over decadal timescales: The



574 role of medium-energy electrons. *Journal of Geophysical Research: Atmospheres*, 123, 607–  
575 622. <https://doi.org/10.1002/2017JD027605>

576

577 Baker, D. N., Mazur, J. E., & Mason, G., (2012). SAMPEX to reenter atmosphere: Twenty-year  
578 mission will end. *Space Weather*, 10, S05006, doi:10.1029/2012SW000804

579

580 Belakhovsky, V.B., Pilipenko, V.A., Antonova, E.E. et al. (2023). Relativistic electron flux  
581 growth during storm and non-storm periods as observed by ARASE and GOES satellites. *Earth  
582 Planets Space* 75, 189, <https://doi.org/10.1186/s40623-023-01925-1>

583

584 Blum, L., Li, X., & Denton, M., (2015). Rapid MeV electron precipitation as observed by  
585 SAMPEX/HILT during high-speed stream-driven storms. *J. Geophys. Res. Space  
586 Physics*, 120, 3783–3794, doi:10.1002/2014JA020633

587

588 Brasseur, G., & Solomon, S., (2005). *Aeronomy of the Middle Atmosphere*, 3rd ed., D. Reidel  
589 Dordrecht, Netherlands.

590

591 Carpenter, D. L., & Anderson, R. R., (1992). An ISEE/whistler model of equatorial electron  
592 density in the magnetosphere. *J. Geophys. Res.*, 97(A2), 1097-1108, doi:10.1029/91JA01548

593

594 Cresswell-Moorcock, K., Rodger, C. J., Kero, A., Collier, A. B., Clilverd, M. A., Häggström, I.,  
595 & Pitkänen, T., (2013). A reexamination of latitudinal limits of substorm-produced energetic  
596 electron precipitation. *J. Geophys. Res. Space Physics*, 118, 6694–6705, doi:10.1002/jgra.50598

597

598 Cussac, T., Clair, M.-A., Pascale, U.-G., Buisson, F., Gerard, L.-B., Ledu, M., et al. (2006). The  
599 Demeter microsatellite and ground segment. *Planetary and Space Science*, 54(5), 413–  
600 427. <https://doi.org/10.1016/j.pss.2005.10.013>

601

602 Dietrich, S., Rodger, C. J., Clilverd, M. A., Bortnik, J., & Raita, T., (2010). Relativistic  
603 microburst storm characteristics: Combined satellite and ground-based observations. *J. Geophys.*  
604 *Res.*, 115, A12240, doi:10.1029/2010JA015777

605

606 Douma, E., Rodger, C. J., Blum, L. W., & Clilverd, M. A., (2017). Occurrence characteristics of  
607 relativistic electron microbursts from SAMPEX observations. *J. Geophys. Res. Space Physics*,  
608 122, 8096–8107, doi:[10.1002/2017JA024067](https://doi.org/10.1002/2017JA024067)

609

610 Douma, E., Rodger, C. J., Blum, L. W., O'Brien, T. P., Clilverd, M. A., & Blake, J. B. (2019).  
611 Characteristics of relativistic microburst intensity from SAMPEX observations. *Journal of*  
612 *Geophysical Research: Space Physics*, 124, 5627–5640. <https://doi.org/10.1029/2019JA026757>

613

614 Evans, D. S., & Greer, M. S. (2006). *Polar Orbiting Environmental Satellite Space Environment*  
615 *Monitor–2 Instrument descriptions and archive data documentation*, NOAA Tech. Mem. 1.4,  
616 (SEM2v2.0.doc, rev 2006). Boulder, Colorado: Space Environ. Lab.

617

618 Forsyth, C., Rae, I. J., Coxon, J. C., Freeman, M. P., Jackman, C. M., Gjerloev, J., & Fazakerley,  
619 A. N. (2015). A new technique for determining substorm onsets and phases from indices of the

620 electrojet (SOPHIE). *Journal of Geophysical Research: Space Physics*, 120, 10592–10606.

621 <https://doi.org/10.1002/2015JA021343>

622

623 Hendry, A. T., Rodger, C. J., & Clilverd, M. A. (2017). Evidence of sub-MeV EMIC-driven

624 electron precipitation. *Geophys. Res. Lett.*, 44, 1210–1218, doi:10.1002/2016GL071807

625

626 Jaynes, A. N., et al. (2015). Source and seed populations for relativistic electrons: Their roles in

627 radiation belt changes. *J. Geophys. Res. Space Physics*, 120, 7240–7254,

628 doi:10.1002/2015JA021234

629

630 Klecker, B., et al., (1993). HILT: a heavy ion large area proportional counter telescope for solar

631 and anomalous cosmic rays. *IEEE Transactions on Geoscience and Remote Sensing*, vol. 31, no.

632 3, pp. 542-548, doi: 10.1109/36.225520

633

634 Macmillan, S., & Maus, S. (2005). International Geomagnetic Reference Field—the tenth

635 generation. *Earth Planet Sp* 57, 1135–1140, <https://doi.org/10.1186/BF03351896>

636

637 Matthes, K. et al., (2017). Solar forcing for CMIP6 (v3.2), *Geosci. Model Dev.*, 10, 2247–2302,

638 <https://doi.org/10.5194/gmd-10-2247-2017>

639

640 Nakamura, R., Kamei, K., Kamide, Y., Baker, D. N., Blake, J. B., & Looper, M., (1998).

641 SAMPEX observations of storm-associated electron flux variations in the outer radiation belt. *J.*

642 *Geophys. Res.*, 103(A11), 26261–26269, doi:10.1029/97JA02873

643

644 Nesse Tyssøy, H, Partamies, N., Babu, E. M., Smith-Johnsen, C., & Salice, J. A. (2021). The  
645 predictive capabilities of the auroral electrojet index for medium energy electron precipitation.  
646 *Front. Astron. Space Sci.* 8:714146. doi: 10.3389/fspas.2021.714146

647

648 O'Brien, T. P., & Moldwin, M. B., (2003). Empirical plasmopause models from magnetic  
649 indices, *Geophys. Res. Lett.*, 30, 1152, doi:10.1029/2002GL016007, 4

650

651 Peck, E. D., Randall, C. E., Green, J. C., Rodriguez, J. V., & Rodger, C. J., (2015). POES  
652 MEPED differential flux retrievals and electron channel contamination correction, *J. Geophys.*  
653 *Res. Space Physics*,120,4596–4612, doi:10.1002/2014JA020817

654

655 Ripoll, J.-F., Claudepierre, S. G., Ukhorskiy, A. Y., Colpitts, C., Li, X., Fennell, J., & Crabtree,  
656 C. (2020). Particle Dynamics in the Earth's Radiation Belts: Review of Current Research and  
657 Open Questions. *Journal of Geophysical Research: Space Physics*, 125, e2019JA026735.  
658 <https://doi.org/10.1029/2019JA026735>

659

660 Rodger, C. J., Clilverd, M. A., Green, J. C., & Lam, M. M. (2010a). Use of POES SEM-2  
661 observations to examine radiation belt dynamics and energetic electron precipitation into the  
662 atmosphere. *Journal of Geophysical Research*, 115(A4), A04202.

663 <https://doi.org/10.1029/2008JA014023>

664

665 Rodger, C. J., Carson, B. R., Cummer, S. A., Gamble, R. J., Clilverd, M. A., Green, J. C., et al.  
666 (2010b). Contrasting the efficiency of radiation belt losses caused by ducted and nonducted

667 whistler-mode waves from ground-based transmitters. *Journal of Geophysical Research*,  
668 115(A12), A12208. <https://doi.org/10.1029/2010JA015880>

669

670 Rodger, C. J., Cresswell-Moorcock, K., & Clilverd, M. A. (2016). Nature's Grand Experiment:  
671 Linkage between magnetospheric convection and the radiation belts. *J. Geophys. Res. Space*  
672 *Physics*, 121, 171–189, doi:10.1002/2015JA021537

673

674 Rodger, C. J., Clilverd, M. A., Hendry, A. T., & Forsyth, C. (2022). Examination of radiation  
675 belt dynamics during substorm clusters: Magnetic local time variation and intensity of  
676 precipitating fluxes. *Journal of Geophysical Research: Space Physics*, 127, e2022JA030750.  
677 <https://doi.org/10.1029/2022JA030750>

678

679 Sauvaud, J.-A, Moreau, T., Maggiolo, R., Treilhou, J., Jacquy, C., Cros, A., Coutelier, J.,  
680 Rouzard, J., Penou, E., & Gangloff, M., (2006). High-energy electron detection onboard  
681 DEMETER: The IDP spectrometer, description and first results on the inner belt. *PSS*, 54(5),  
682 doi:10.1016/j.pss.2005.10.019

683

684 Shprits, Y. Y., Meredith, N. P., & Thorne, R. M., (2007). Parameterization of radiation belt  
685 electron loss time scales due to interaction with chorus waves. *Geophysical Research Letters*, 34.  
686 <https://doi.org/10.1029/2006GL029050>

687

688 Simms, L., Engebretson, M., Clilverd, M., Rodger, C., Lessard, M., Gjerloev, J., & Reeves, G.  
689 (2018). A distributed lag autoregressive model of geostationary relativistic electron fluxes:

690 Comparing the influences of waves, seed and source electrons, and solar wind inputs. *Journal of*  
691 *Geophysical Research: Space Physics*, 123, 3646–3671, <https://doi.org/10.1029/2017JA025002>

692

693 Thomsen, M. F., (2004). Why Kp is such a good measure of magnetospheric convection. *Space*  
694 *Weather*, 2, S11004, doi:10.1029/2004SW000089

695

696 Usanova, M. E., et al. (2014). Effect of EMIC waves on relativistic and ultra relativistic electron  
697 populations: Ground-based and Van Allen Probes observations. *Geophys. Res. Lett.*, 41, 1375–  
698 1381, doi:10.1002/2013GL059024

699

700 van de Kamp, M., Seppälä, A., Clilverd, M. A., Rodger, C. J., Verronen, P. T., & Whittaker, I.  
701 C., (2016). A model providing long-term data sets of energetic electron precipitation during  
702 geomagnetic storms. *J. Geophys. Res. Atmos.*, 121, 12,520–12,540, doi:10.1002/2015JD024212

703

704 Wanliss, J. A., & Showalter, K. M., (2006). High-resolution global storm index: Dst versus  
705 SYM-H. *J. Geophys. Res.*, 111, A02202, doi:10.1029/2005JA011034

706

707 Whittaker, I. C., Gamble, R. J., Rodger, C. J., Clilverd, M. A., & Sauvaud, J.-A., (2013).

708 Determining the spectra of radiation belt electron losses: Fitting DEMETER electron flux  
709 observations for typical and storm times. *J. Geophys. Res. Space Physics*, 118, 7611–7623,

710 doi:10.1002/2013JA019228

711

712 Whittaker, I.C., Clilverd, M.A., & Rodger, C. J., (2014). Characteristics of precipitating  
713 energetic electron fluxes relative to the plasmopause during geomagnetic storms. *J. Geophys.*  
714 *Res. Space Physics*, 119, 8784–8800, doi:10.1002/2014JA020446

715

716 Yando, K., Millan, R. M., Green, J. C., & Evans, D. S., (2011). A Monte Carlo simulation of the  
717 NOAA POES Medium Energy Proton and Electron Detector instrument. *J. Geophys. Res.*, 116,  
718 A10231, doi:10.1029/2011JA016671

719

720 Zhao, H., & Li, X., (2013). Inward shift of outer radiation belt electrons as a function of Dst  
721 index and the influence of the solar wind on electron injections into the slot region. *J. Geophys.*  
722 *Res. Space Physics*, 118, 756–764, doi:10.1029/2012JA018179.

723

724 Captions

725

726 **Figure 1.** World map showing the changing radiation belt electron flux population observed by  
727 the three different satellites considered in this study. The upper panel is for DEMETER adapted  
728 from Whittaker et al. (2013), the middle panel is the 90° telescope carried onboard the POES  
729 SEM-2 constellation adapted from Rodger et al. (2010b), and the lower panel is for SAMPEX  
730 HILT adapted from Dietrich et al. (2010). Here T indicates trapped flux, DLC is drift-loss cone,  
731 and FL BLC is field line bounce loss cone. For most locations where there is a significant  
732 radiation belt flux, it observes a mix of DLC and FL BLC populations. The green boxes show the  
733 spatial regions selected in the current study to investigate EEP in DEMETER, 90° telescope  
734 POES, and SAMPEX HILT.

735

736 **Figure 2.** DEMETER IDP electron flux data from an example half orbit on 6 May 2006  
737 displayed in 0.25-wide L-shell bins. Evidence of quantisation of low flux values near the  
738 instrument measurement floor is apparent (e.g., values occurring below the solid black line).

739

740 **Figure 3.** The calculated noise floor plotted as a solid black line on top of a series of energy  
741 spectra taken from an example DEMETER half orbit on 6 May 2006. The effective noise floor,  
742 based on a threshold of 2 counts/s in the IDP detector has been used to discard unreliable flux  
743 values.

744

745 **Figure 4.** The variation of DEMETER >90 keV electron precipitation fluxes with L-shell and  
746 geomagnetic activity. Four panels represent the AE, Kp, Dst, and Ap index variations. The black

747 lines indicate the location of the plasmapause for three of the different geomagnetic indices,  
748 using the formulations given in O'Brien and Moldwin (2003).

749

750 **Figure 5.** The variation of POES >100 keV electron precipitation fluxes with L-shell and  
751 geomagnetic activity, for the 90° detector viewing the North Atlantic sample region, in the same  
752 format as Figure 4.

753

754 **Figure 6.** The variation of POES >100 keV 0° detector electron precipitation fluxes with L-shell  
755 and geomagnetic activity. In this case all longitudes are included. Otherwise the plot is in the  
756 same format as Figure 4.

757

758 **Figure 7.** As for Figure 4, but plotting > 700 keV DEMETER electron precipitation fluxes in the  
759 North Atlantic sampling region.

760

761 **Figure 8.** The variation of SAMPEX HILT >1.05 MeV electron precipitation fluxes with L-shell  
762 and geomagnetic activity, for the North Atlantic sample region. Same format as Figures 4 to 7.

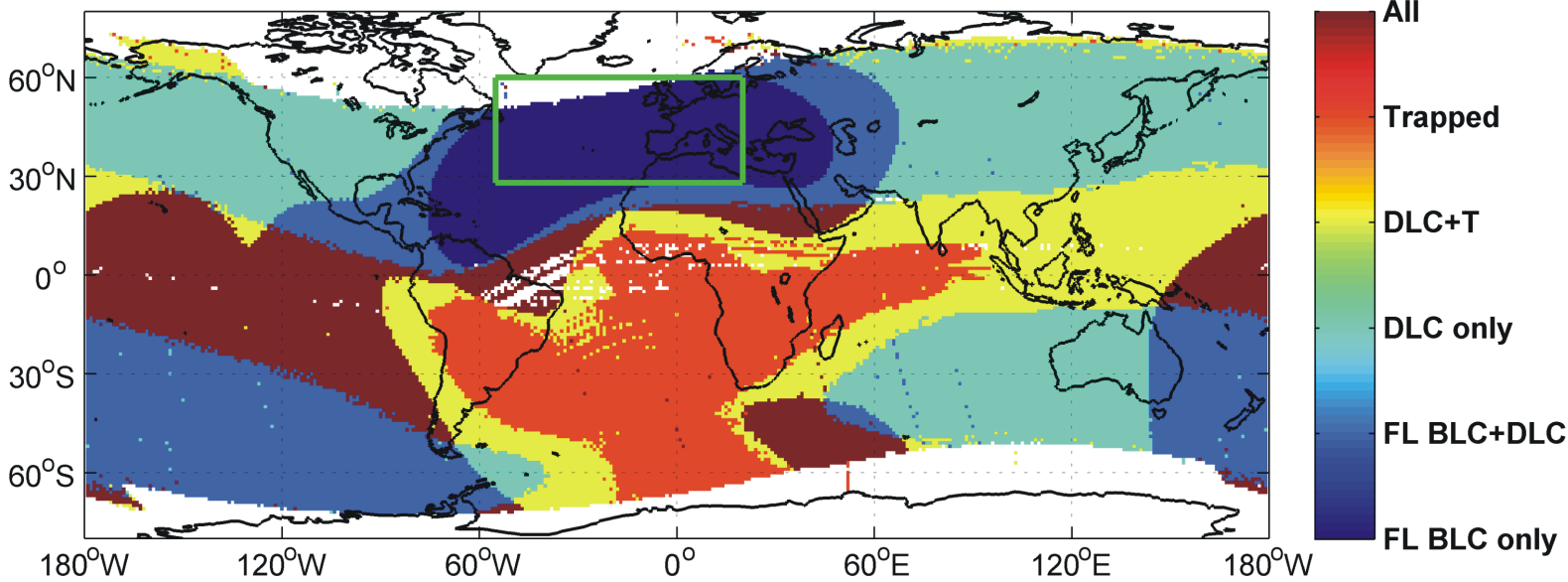
763

764 **Figure 9.** The variation of POES SEM-2 E4 0° detector >700 keV electron precipitation fluxes  
765 with L-shell and geomagnetic activity. This includes observations from all longitudes, in the  
766 same format as Figure 8.

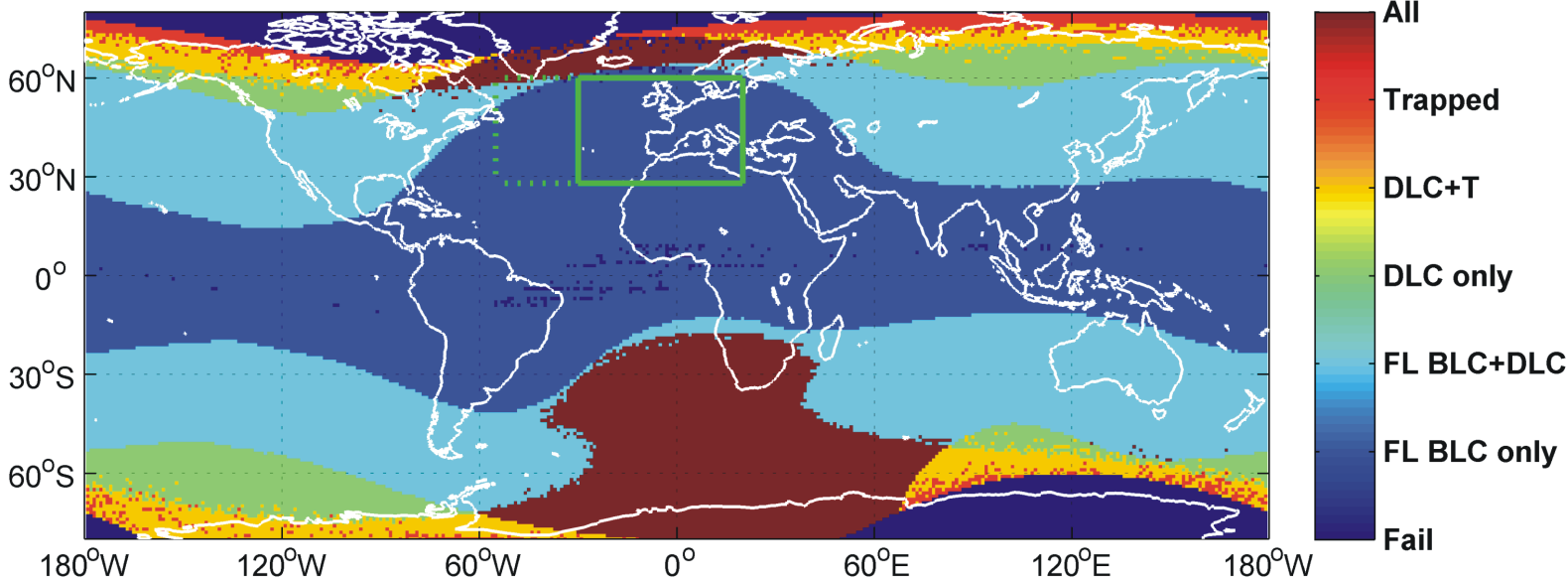


Figure1.

# DEMETER Radiation Belt Populations



# POES 90-degree Radiation Belt Populations



# SAMPEX Radiation Belt Populations

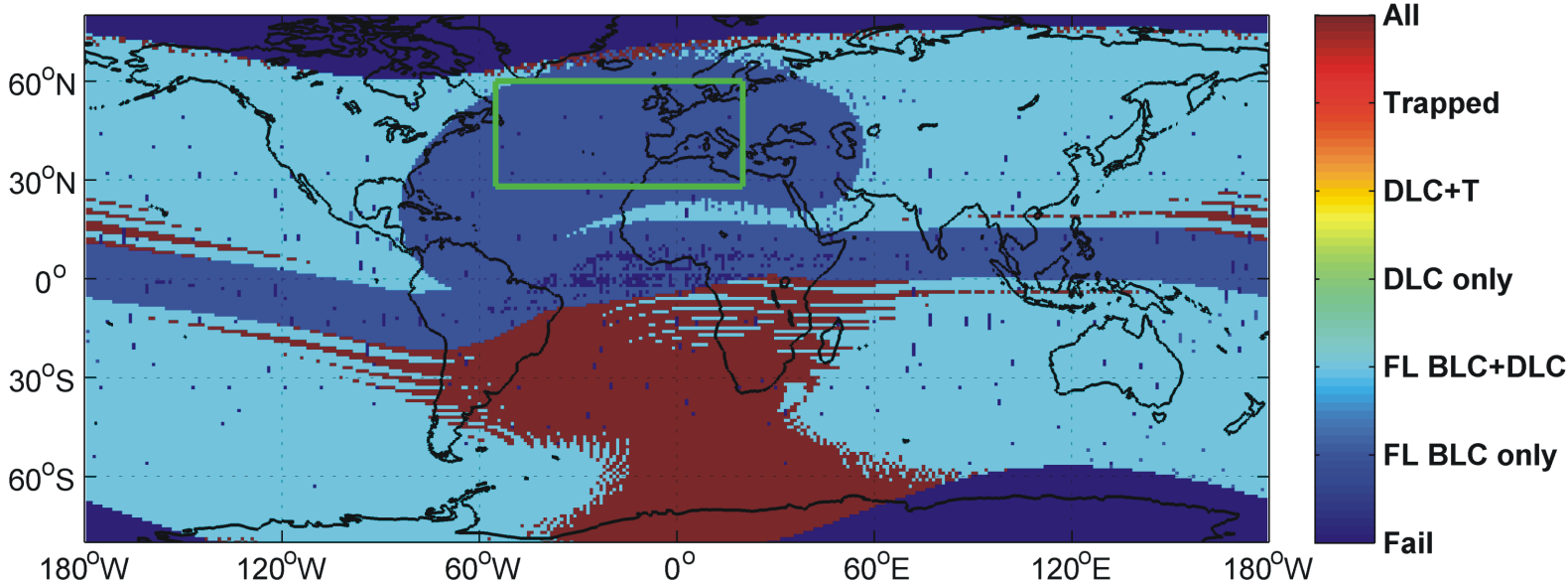


Figure 2.

DEMETER half-orbit #09818.5, 6 May 2006

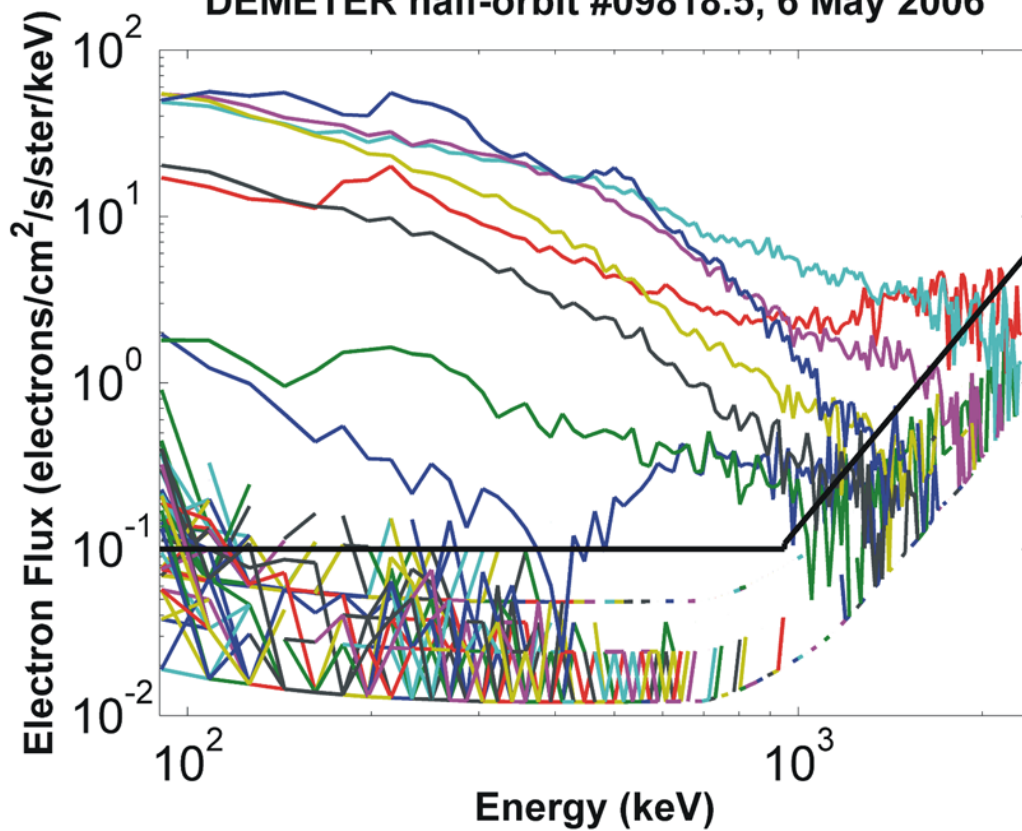


Figure 3.

DEMETER half-orbit #09818.5, 6 May 2006

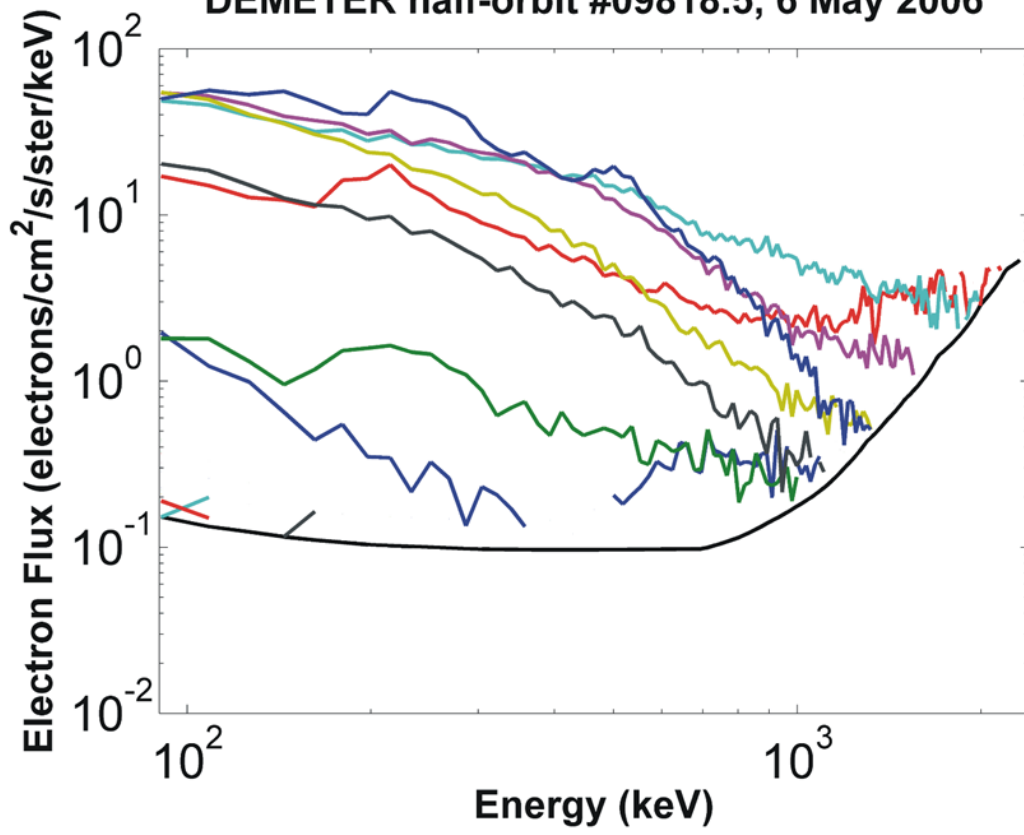


Figure 4.

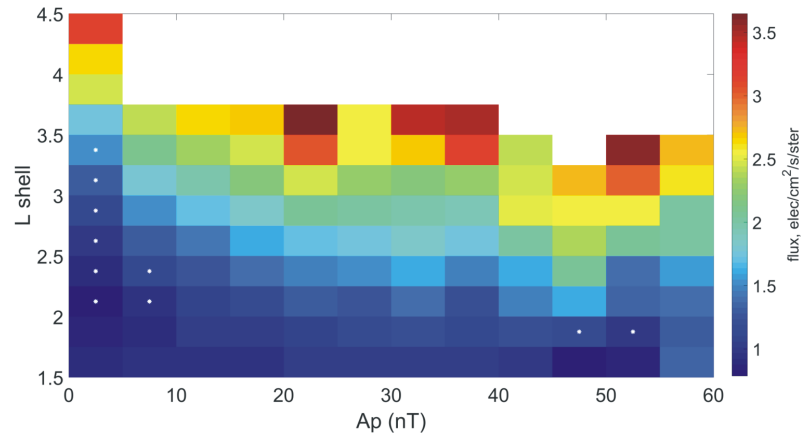
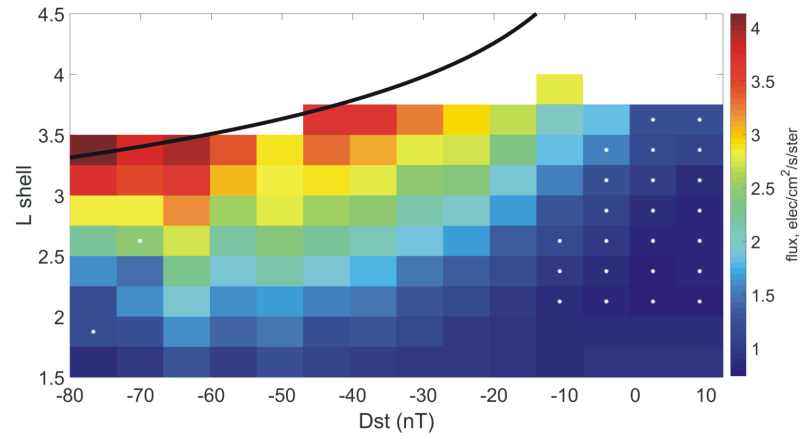
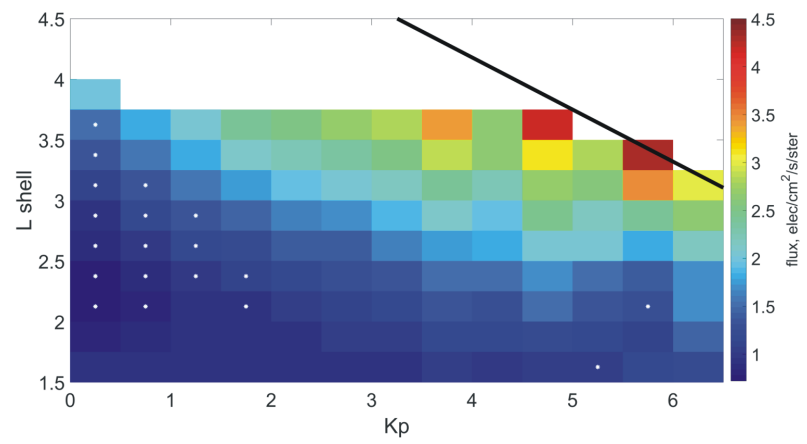
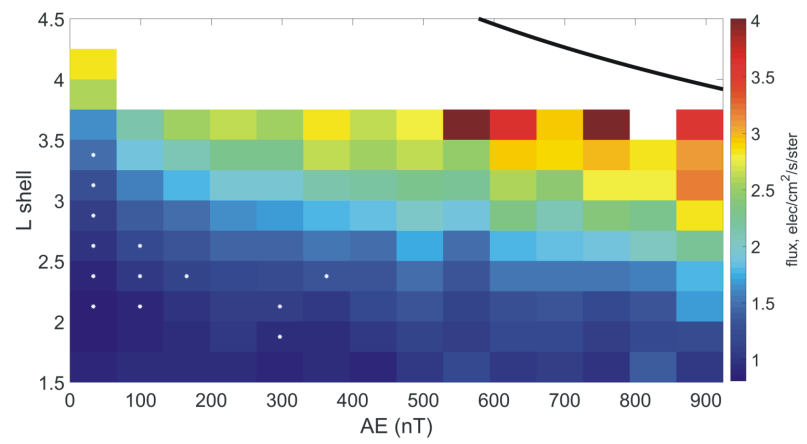




Figure 5.

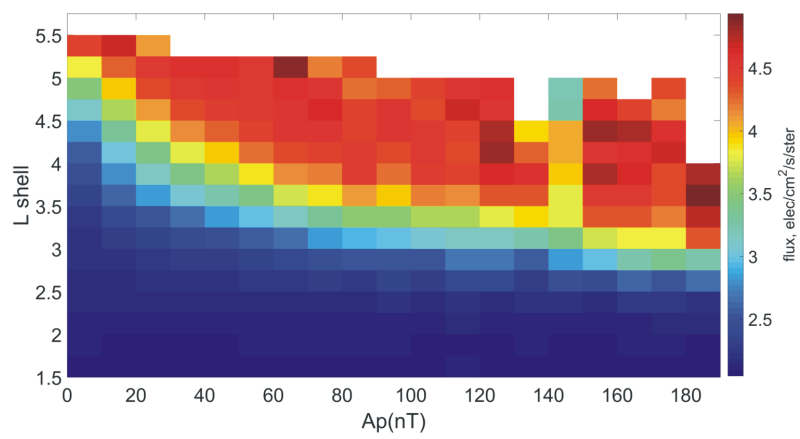
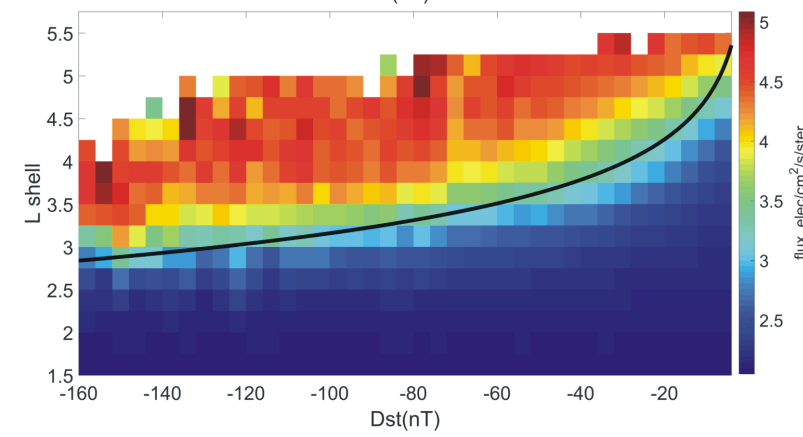
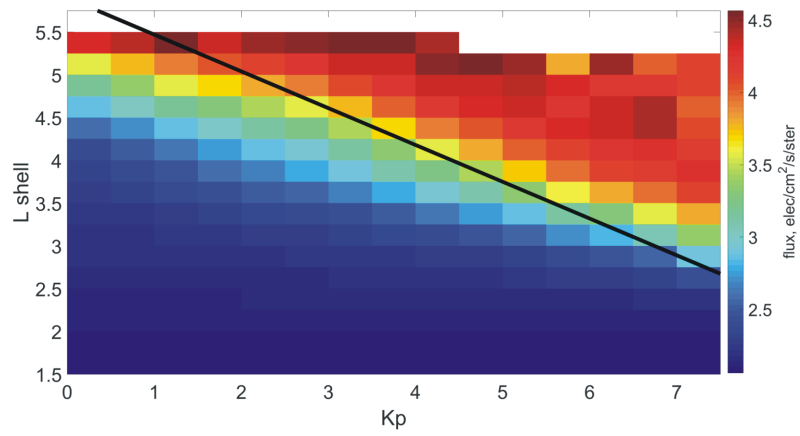
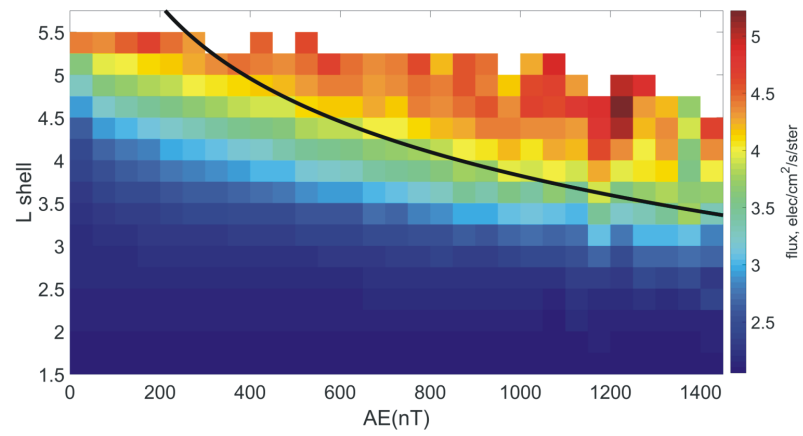


Figure 6.

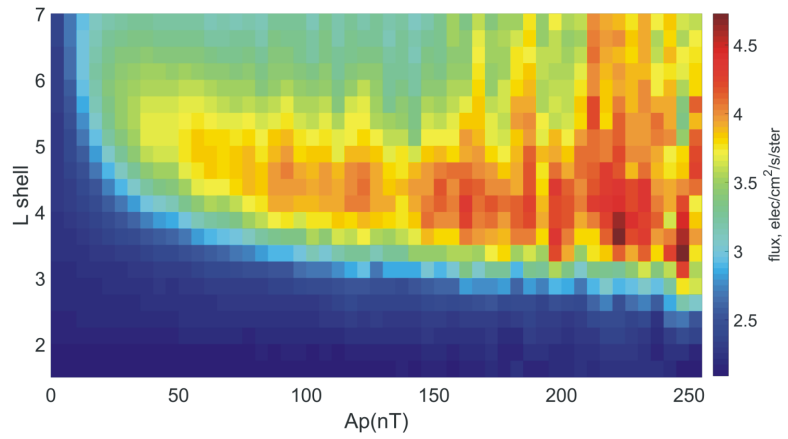
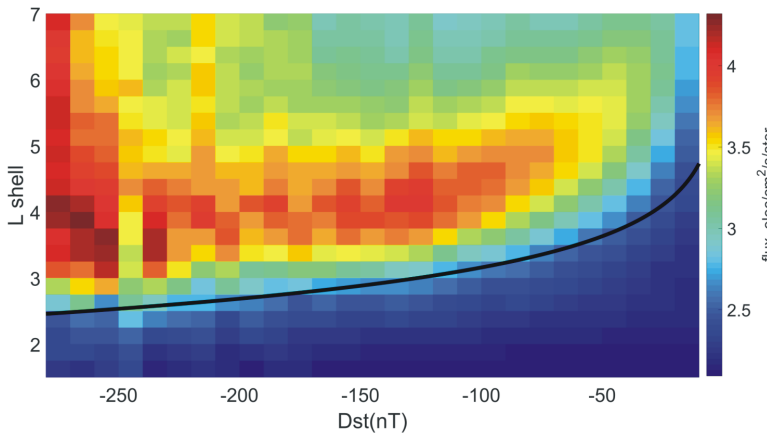
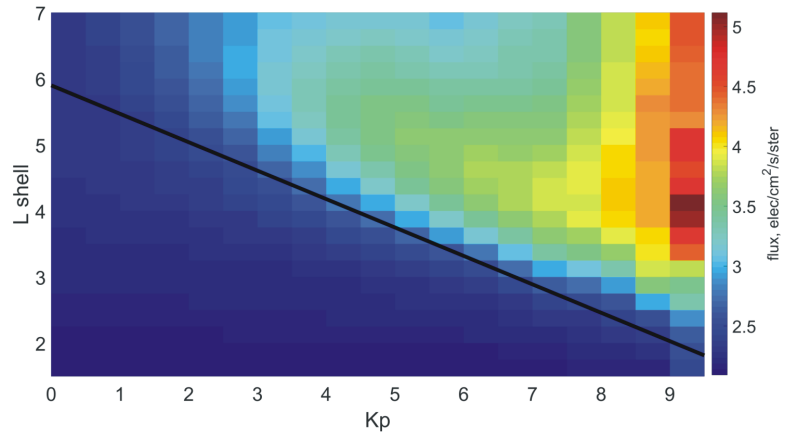
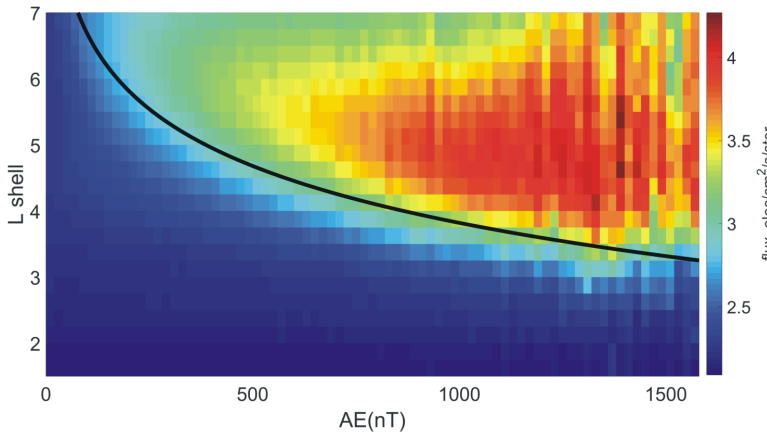


Figure 7.

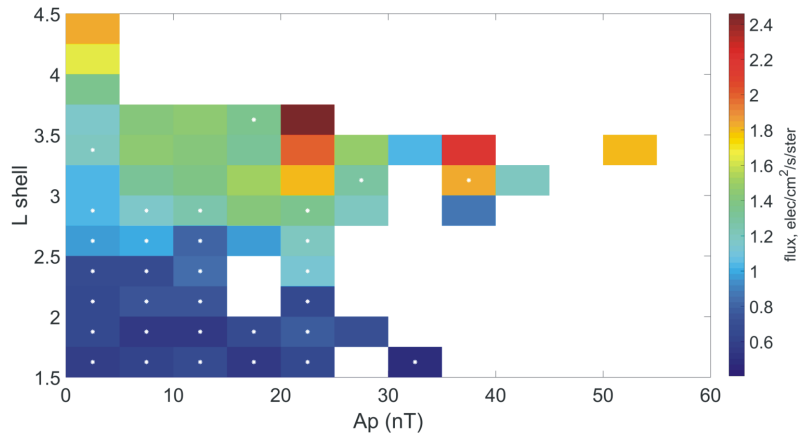
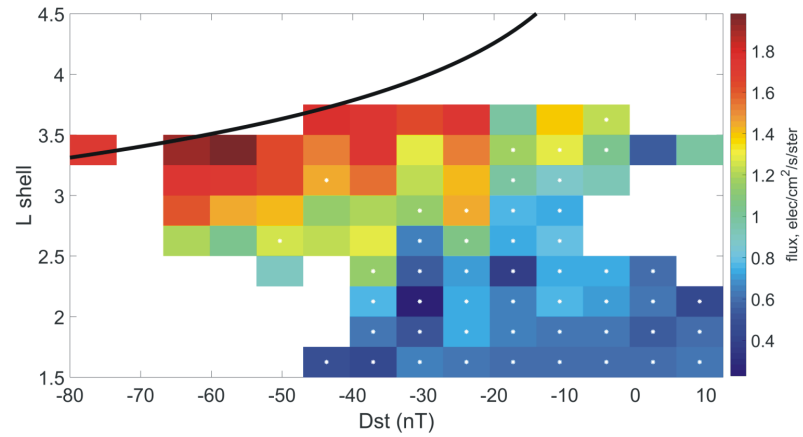
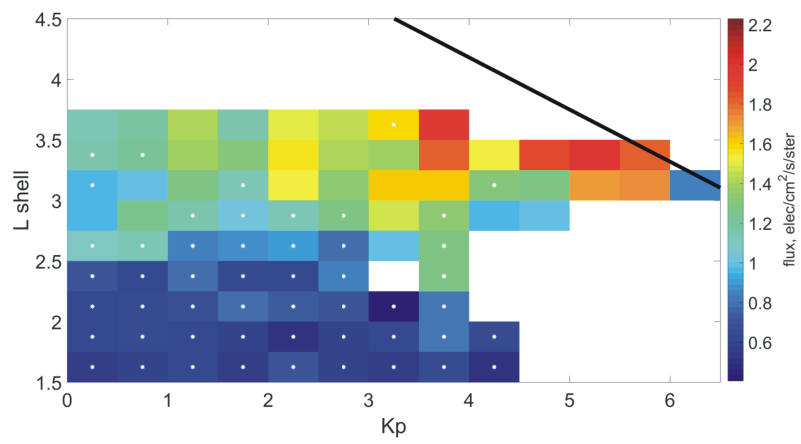
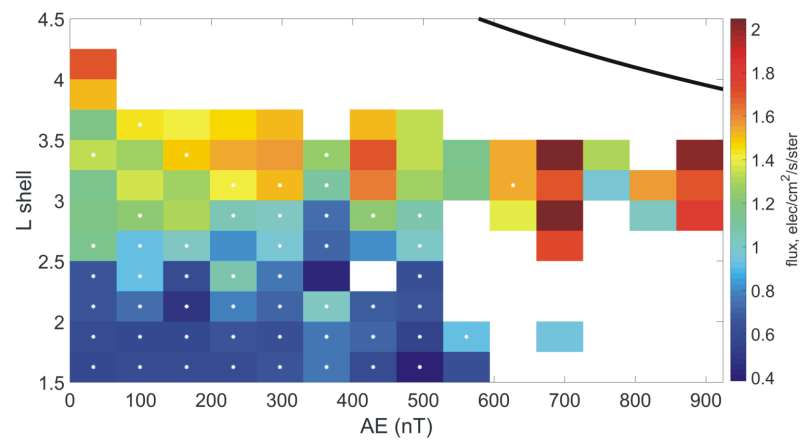


Figure 8.

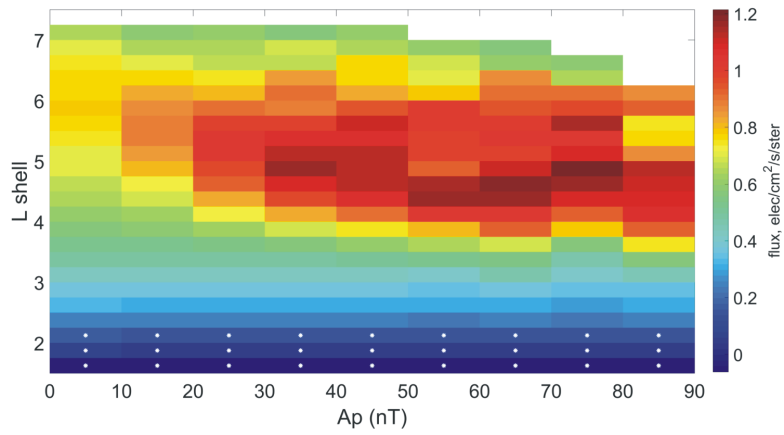
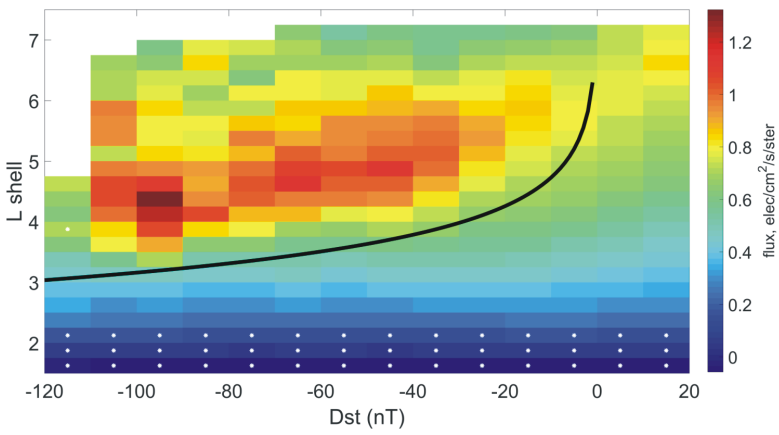
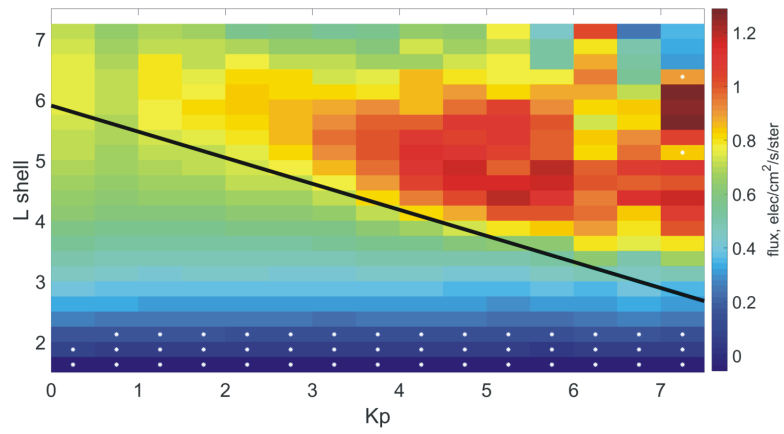
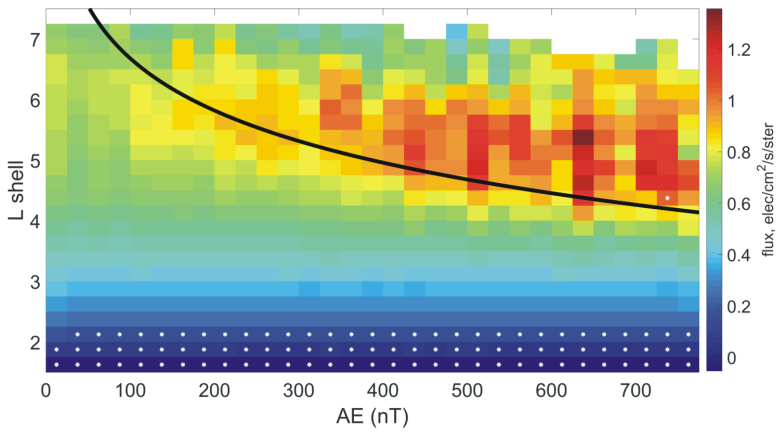




Figure 9.

